

Modeling and Simulation of Valve Cycle in Vein Using an Immersed Finite Element Method

Xiang Liu¹, Liangbo Sun², Mingzhen Wang^{3,4}, Bin Li² and Lisheng Liu^{1,5,*}

Abstract: A vein model was established to simulate the periodic characteristics of blood flow and valve deformation in blood-induced valve cycles. Using an immersed finite element method which was modified by a ghost fluid technique, the interaction between the vein and blood was simulated. With an independent solid solver, the contact force between vein tissues was calculated using an adhesive contact method. A benchmark simulation of the normal valve cycle validated the proposed model for a healthy vein. Both the opening orifice and blood flow rate agreed with those in the physiology. Low blood shear stress and maximum leaflet stress were also seen in the base region of the valve. On the basis of the healthy model, a diseased vein model was subsequently built to explore the sinus lesions, namely, fibrosis and atrophy which are assumed stiffening and softening of the sinus. Our results showed the opening orifice of the diseased vein was inversely proportional to the corresponding modulus of the sinus. A drop in the transvalvular pressure gradient resulted from the sinus lesion. Compared to the fibrosis, the atrophy of the sinus apparently improved the vein deformability but simultaneously accelerated the deterioration of venous disease and increased the risk of potential fracture. These results provide understandings of the normal/abnormal valve cycle in vein, and can be also helpful for the prosthesis design.

Keywords: Numerical simulation, fluid-structure interaction, immersed finite element method, adhesive contact method, bio-mechanics, venous valve.

1 Introduction

Venous disorders have attracted considerable attention in recent times due to their high prevalence and economic burden [Meissner, Moneta, Burnand et al. (2007)]. An epidemiological survey in the United States showed that nearly 35% of the adults had varicose veins [McLafferty, Passman, Caprini et al. (2008)], while the annual medical

¹ Department of Engineering Structure and Mechanics, Wuhan University of Technology, Wuhan, 430070, China.

² College of Mechanical Engineering, Wuhan Polytechnic University, Wuhan, 430048, China.

³ China Special Vehicle Research Institute, Aviation Key Scientific and Technological Laboratory of High Speed Hydrodynamic, Jingmen, 448035, China.

⁴ Nanjing University of Aeronautics and Astronautics, Nanjing, 210016, China.

⁵ State Key Laboratory of Advanced Technology of Materials Synthesis and Processing, Wuhan University of Technology, Wuhan, 430070, China.

* Corresponding Author: Lisheng Liu. Email: liulish@whut.edu.cn.

Received: 07 October 2019; Accepted: 16 January 2020.

expenditure on chronic venous diseases (CVD) was more than 100 million euros per million inhabitants in Europe [Carpentier, Maricq, Biro et al. (2004)]. Diseased veins have been studied using both *in vivo* [Hertzberg, Kliewer, DeLong et al. (1997); Yamaki, Sasaki and Nozaki (2002)] and *in vitro* [Buescher, Nachiappan, Brumbaugh et al. (2005); Lurie, Kistner, Eklof et al. (2003)] models, as well as mathematical simulation. Although *in vivo* imaging could display pathological symptoms [Lurie, Kistner, Eklof et al. (2003)], such as vascular lesion [Hertzberg, Kliewer, DeLong et al. (1997)], valve lesion [Yamaki, Sasaki and Nozaki (2002)] and sinus lesion [Korch, Cuvinciuc, Caetano (2014)], the analyses were only qualitative. With artificial venous flow systems, it was possible to calculate the kinetics of venous movement and blood flow, as well as quantify the effects of abnormal valve anatomy [Buescher, Nachiappan, Brumbaugh et al. (2005)]. Nevertheless, dynamic measurements were still challenging in *in vivo* and *in vitro* experiments [Qui, Quijano, Wang et al. (1995)].

Finite element modeling allows the flexible, reproducible and quantitative analysis of multifactorial scenarios [Zervides and Giannoukas (2013)]. Mathematical studies of heart valve [Aluri and Chandran (2001); Li, Baird, Yao et al. (2019)] and aortic valve [Bavo, Rocatello, Iannaccone et al. (2016)] have successfully revealed both the kinetic and dynamic characteristics of the interaction between biological motions and blood. Therefore, modeling and simulation of the venous valve cycle are of interest in clinical diagnosis as well as in bio-engineering applications.

So far, only a few reports were available on the finite element modeling of veins [Buxton and Clarke (2007); Chen, Berwick, Krieger et al. (2014)]. Buxton et al. [Buxton and Clarke (2007)] used a lattice spring model to illustrate the basic physics of vein valves. They investigated the dynamics of the valve opening area, and captured the unidirectional nature of the blood flow across the venous valve. Subsequently, Chen et al. [Chen, Berwick, Krieger et al. (2014)] reported a biomechanical comparison between mono-, bi- and tri-cuspid venous valve architectures. They provided the relevant implications on the structure and flow mechanics in the vein and found that the mechanical cost for the bicuspid valve was lowest. In these modellings, the employed dimensions were not based on physiological data, and the wall was assumed as a rigid tube without a sinus structure.

Recently, researchers began to propose numerical models for the studies related to CVD. Simão et al. [Simão, Ferreira, Mora et al. (2016)] built an Arbitrary Lagrangian-Eulerian (ALE) model for the vein blockage induced by a deep venous thrombosis. They captured the abnormal venous valve operation and the clot formation, verified some results of the fluid mechanics and the valves dynamics using the *in vivo* measurements. Soifer et al. [Soifer, Weiss, Marom et al. (2016)] also established an ALE model of a diseased vein model, and studied the effect of the fibrotic valve on its neighboring valve. Ariane et al. [Ariane, Wen, Vigolo et al. (2017)] developed a discrete multi-physics model and captured the hemodynamics in flexible deep veins valves. Chen et al. [Chen, Diaz, Fedor et al. (2018)] investigated the helical flow owing to the relative orientation and spacing of the valves, using an ALE vein model. In those researches, the body-fitted technique was almost employed by all. The modeling results scarcely exhibited the realistically finite deformation. The pathological cases were mostly related to the stiffening of the leaflet, and the wall was also fixed. The lesion of the sinus has been rarely concerned in the

above studies even though it plays a significant role in the dynamics of blood [Tien, Chen, Berwick et al. (2014a)].

Based on these findings, we established a non-body-fitted two-dimensional (2-D) vein model by a modified immersed finite element method (IFEM) combined with adhesive contact method (ACM) [Fan, Ren and Li (2015)]. This modified IFEM is on the basis of the original IFEM [Zhang, Gerstenberger, Wang et al. (2004)]. Similarly to the previous IFEM studies of the smoothed solid solver in IS-FEM [Zhang, Liu and Khoo (2013)], the improved iteration in semi-implicit IFEM [Wang, Wang and Zhang (2012)], the balance of discrepancy in the FSI [Wang and Zhang (2013)] and the open-sourced implementation of mIFEM [Cheng, Yu and Zhang (2019)], there were some modifications in this method. An independent solid constitution and solver was employed so that the solid was driven by the hydrodynamic forces, which enabled the fluid-structure interaction (FSI) [Li and Wang (2019); Wang, Yang and Wu (2019)] in the original IFEM to approximate to the real physics. We also introduced the concept of the Ghost Fluid [Fedkiw, Aslam, Merriman et al. (1999)] into the employed IFEM, so the influence of non-physical fluid on the N-S equations could be decreased. The interpolations were then imposed only on the solid boundary and the immersed interface. And the computations of the FSI was accelerated and improved. The finite element modeling of heart valves [Aluri and Chandran (2001)] has revealed that pressure and velocity fields of the three-dimensional (3-D) model and 2-D model are comparable. Thus, the 2-D finite element modeling was more computationally efficient for this numerical study.

Following our previous study on the effect of the valve lesion [Liu and Liu (2019a)], a prospective study was then conducted to explore how the pathological stiffening and softening of the sinus changed the valve functioning. The vein was designed to be immersed in an independent of the background fluid domain. To mimic the periodic opening-closing behavior of the valves, the blood-vein interaction [Yao, Liu, Narmoneva et al. (2012)] was modeled via interpolation in the IFEM, the contact action between the leaflets [Zeng and Li (2012)] was achieved by the ACM. As one common etiology of tissues was abnormal elastic properties, the softening and stiffening were both used to determine the sinus lesion in this work.

Based on the proposed FSI method, we simulated a blood-induced venous valve cycle using a computational model. In the present study, the results of valve orifice, fluid velocity, and pressure were gained, and then compared with the existing experimental and theoretical results to verify the proposed model. Additionally, the effects of venous sinus lesions [Dydek and Chaikof (2016); Simmons, Grant, Manduchi et al. (2005)] on the vein performance were further analyzed by comparing the healthy and diseased cases. To be clearly illustrated, this paper composed of the following sections. In Section 2, we introduce the employed numerical algorithms and computational techniques. In Section 3, we describe the finite element modeling, along with parameters of the healthy vein and pathological vein. In Section 4, the computational results of the veins will be summarized, and we give the discussion. In Section 5, we draw a relevant conclusion.

2 Numerical method

2.1 Immersed finite element method

2.1.1 Governing equations

In the IFEM, a physical domain Ω usually includes a fluid in Ω^f and an immersed solid in Ω^s , as shown in Fig. 1. In the computation, a Eulerian fluid mesh is adopted in Ω ; a Lagrangian solid mesh in Ω^s is constructed on top of Ω . The fluid mesh spanning over Ω is continuous. There are two physical spaces in the coordinate system: $\mathbf{x} \in \Omega \subset \mathcal{R}^d$ denotes the Cartesian coordinate of the Eulerian fluid and $\mathbf{X}^s \in \Omega^s \subset \mathcal{R}^d$ the Lagrangian positions of the solid. For the fluid-solid coupling, the Cartesian coordinate of the solid position \mathbf{X}^s at time t is mapped into $\mathbf{x}^s(\mathbf{X}^s, t)$.

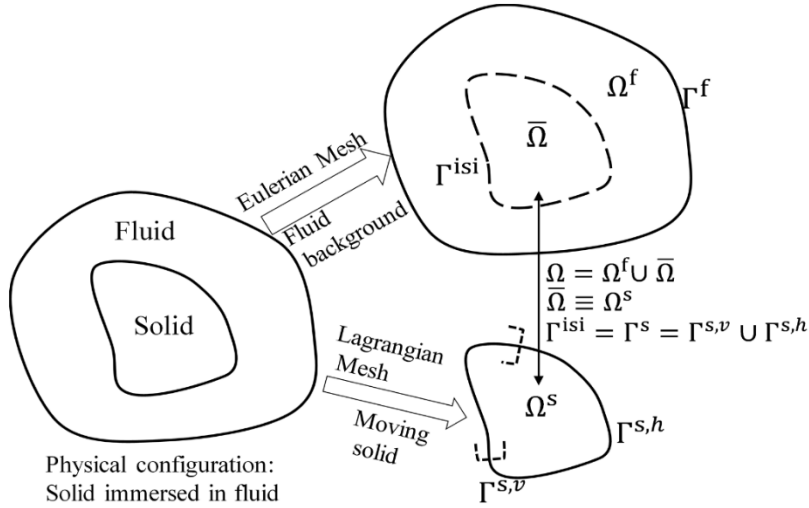


Figure 1: Description of the solid and fluid domain in the IFEM [Wang and Zhang (2013)]. Here the artificial fluid is employed in the previous IFEM then $\bar{\Omega} = \Omega^v$

When the fluid is incompressible and Newtonian, and the hydrodynamics are described by the N-S equations:

$$\begin{cases} v_{j,j} = 0 \\ \rho \dot{v}_i + \rho v_j v_{i,j} = \sigma_{i,j} + \rho g_i \end{cases}, \text{ on } \Omega \quad (1)$$

with

$$\sigma_{ij} = p + \mu(v_{i,j} + v_{j,i}), \text{ on } \Omega \quad (2)$$

where ρ is the fluid density, and μ is the dynamic viscosity coefficient; v_j is the velocity, g_i is the acceleration, σ_{ij} is the Cauchy stress, and p is the pressure.

As the entire domain Ω in the previous IFEM is occupied by the artificial fluid in Ω^v and the real fluid in Ω^f , the density in Ω is determined by

$$\rho = \int_{\Omega} \rho^v \varphi(\mathbf{x} - \mathbf{x}^s) d\Omega, \text{ on } \Omega \quad (3)$$

where ρ^v is the density in Ω^v , with $\rho^v = \rho^f$ in the original IFEM [Zhang, Gerstenberger, Wang et al. (2004)] and $\rho^v = \rho^s$ in the m-IFEM [Wang and Zhang (2013)]; $\varphi(\mathbf{x} - \mathbf{x}^s)$ is the reproduced kernel particle function (RKPF).

When the immersed solid is incompressible and elastic, the dynamic equation is written as below:

$$\rho^s \ddot{d}_i^s = \rho^s \dot{v}_i^s = \sigma_{ij,j}^s, \text{ on } \Omega^s \quad (4)$$

where ρ^s is the solid density, v_i^s is the solid velocity $\dot{d}_i^s(\mathbf{x}^s(\mathbf{X}^s, t))$, \ddot{d}_i^s is the solid acceleration $\dot{v}_i^s(\mathbf{x}^s(\mathbf{X}^s, t))$, and σ_{ij}^s is the solid stress.

Owing to the solid overlapping with the artificial fluid, an additional force is discretely interpolated as a coupling force for the coupling between the N-S equations and the dynamic equation. The FSI force is

$$f_i^{\text{fsi},f} = \int_{\Omega^s} f_i^{\text{fsi},s} \varphi(\mathbf{x} - \mathbf{x}^s) d\Omega, \text{ on } \Omega/\Omega^f \text{ and } \Omega^s \quad (5)$$

where $f_i^{\text{fsi},f}$ is a body force term added to Eq. (1). And $f_i^{\text{fsi},s}$ is a solid FSI force calculated as

$$f_i^{\text{fsi},s} = \sigma_{ij,j}^s - \sigma_{ij,j}^f, \text{ on } \Omega/\Omega^f \text{ and } \Omega^s \quad (6)$$

2.1.2 Modification with ghost fluid

As the artificial fluid participates in the solution of the N-S equations and the interpolation in the previous IFEM: the velocity/pressure field of the real fluid is contaminated [Wang and Zhang (2013)]. Again, the introductions of and additional coupling force require a more computational cost. To improve the computation, the artificial fluid is replaced by the ghost fluid [Fedkiw, Aslam, Merriman et al. (1999)] in the proposed IFEM. Then, $\bar{\Omega} = \Omega^s$ could be used in Fig. 1 for illustration. The ghost fluid occupies the domain Ω^g . The material properties in Ω^g are assumed infinitely small.

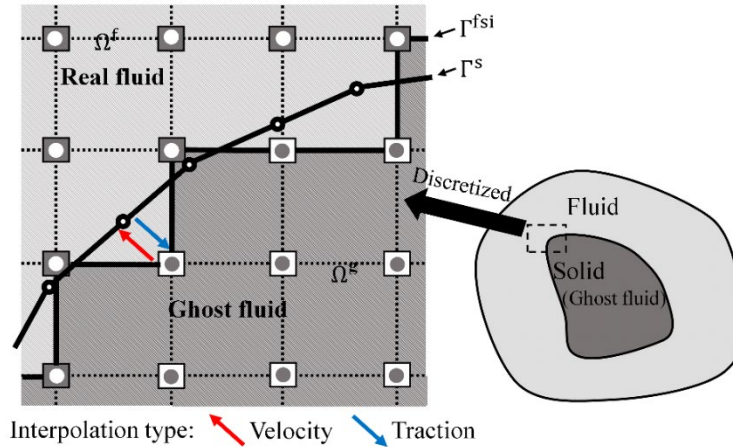


Figure 2: Velocity and traction interpolations of the FSI model

The density ρ in Ω is redefined and Eq. (3) is rewritten as

$$\rho = \int_{\Omega} \rho^f \delta(\mathbf{x} - \mathbf{x}^s) d\Omega, \text{ on } \Omega \quad (7)$$

with

$$\int_{\Omega} \delta(\mathbf{x} - \mathbf{x}^s) d\Omega = \begin{cases} 1, & \mathbf{x} \in \Omega^f \\ 10^{-9}, & \mathbf{x} \in \Omega^g, \end{cases} \text{ on } \Omega \quad (8)$$

where $\delta(\mathbf{x})$ is a Dirac Delta function. The infinitely small properties for the ghost fluid are achieved by multiplying a coefficient 10^{-9} in the numerical implementation. With substituting Eq. (8) into Eq. (1), the solution of the N-S equations is modified. The finite element formulations of the N-S equations are given in Appendix A.

As shown in Fig. 2, the material in Ω^f can be distinguished from that in Ω^g by the immersed (Fluid-Ghost) interface Γ^{fsi} . The degrees of freedom of the ghost fluid nodes are neglected and not counted into the liquid solution. The discrete interpolation like Eq. (5) is also eliminated between Ω^g and Ω^s , without the establishment of the RKPF. The velocity and traction are interpolated directly between Γ^{fsi} and Γ^s in a neighbor-to-neighbor way. The interpolation equations are written as

$$v_i(\mathbf{x}(\Gamma^{\text{fsi}}), t) = v_i^s(\mathbf{X}^s(\Gamma^s, t), t), \text{ on } \Gamma^{\text{fsi}} \text{ and } \Gamma^s \quad (9)$$

$$h_i^s(\mathbf{X}^s(\Gamma^s, t), t) = h_i(\mathbf{x}(\Gamma^{\text{fsi}}), t) = \sigma_{ij}(\mathbf{x}(\Gamma^{\text{fsi}}), t) \cdot n_j, \text{ on } \Gamma^{\text{fsi}}, \Gamma^s \quad (10)$$

where h_i are the fluid traction on the (Fluid-Ghost) interface Γ^{fsi} .

In the solid solver, an implicit formulation of the solid dynamics is employed for stable and convergent solution. Considering the damping effect of the immersed solid, and Eq. (4) is replaced with

$$\sigma_{ij,j}^s - \rho^s \dot{d}_i^s - c \dot{d}_i^s = f_i^s, \text{ on } \Omega^s \quad (11)$$

where c is the damping coefficient. The external force f_i^s is further expressed by $f_i^s = f_i^{s,b,\text{fsi}} + f_i^{s,\text{cont}}$, where $f_i^{s,b,\text{fsi}}$ is the body force term of h_i^s on Γ^s and $f_i^{s,\text{cont}}$ is the body force between solids in the adhesive contact model. The finite element formulation of Eq. (11) is given in Appendix B.

2.2 Adhesive contact method

The contact force between valves is mainly associated with the adhesive contact potential [Fan, Ren and Li (2015)], as illustrated in Fig. 3.

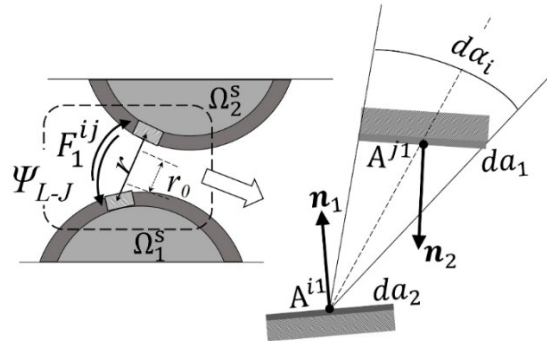


Figure 3: Typical adhesive contact model

The representative adhesive contact model is composed of an i th infinitesimal surface A^{i1} of the solid Ω_1^s and a j th infinitesimal surface B^{j2} of the solid Ω_2^s , F_1^{ij} is the long-range force acting between them and it acts on both Ω_1^s and Ω_2^s ,

$$F_1^{ij} = \beta_1 \beta_2 n_2 da_2 d\alpha_i (-1)^{j+1} \int_{s_{ij}}^{\infty} \phi(r) r^2 dr, \text{ on } A^{i1} \text{ and } A^{j2} \quad (12)$$

where $\phi(r)$ is the adhesion potential, for which a Lennard-Jones potential function is chosen as follows

$$\phi(r) = \epsilon [(r_0/r)^{12} - 2(r_0/r)^6], \text{ on } \Omega_1^s \text{ and } \Omega_2^s \quad (13)$$

In Eqs. (12) and (13), variables can be determined according to Fig. 3, where β_1 and β_2 are the dimensionless particle densities, \mathbf{n}_1 and \mathbf{n}_2 are the normal vectors, da_1 and da_2 are the surface areas, $d\alpha_i$ is the angle of the wedge formed by point B and the facet A^{i1} , ϵ is the potential well, $\mathbf{r} = \mathbf{r}_1 - \mathbf{r}_2$ is the distance vector from Point B to Point A, and r_0 is the equilibrium distance. Detailed mathematical deductions were presented by Fan et al. [Fan, Ren and Li (2015)].

Since F_1^{ij} is expressed in the integral form, $f_i^{s,\text{cont}}$ in Eq. (11) is written as

$$f_i^{s,\text{cont}} = \frac{\partial F_1^{ij}}{\partial V} \quad (14)$$

2.3 Implementation step

The proposed method is implemented in a FORTRAN90 program, and the steps are listed as below:

- The time loop is entered - At time $i\Delta t$, the position of the known solid is $\mathbf{x}^s(\mathbf{X}^s, (i - 1)\Delta t)$, the traction \mathbf{h}^s is transformed into the nodal force $\mathbf{f}^{s,b,\text{fsi}}$, and the contact force $\mathbf{f}^{s,\text{cont}}$ is calculated by Eq. (16). The physical quantities \mathbf{v}^s and $\boldsymbol{\sigma}^s$, $\boldsymbol{\epsilon}^s$ are then solved by Eq. (11).
- On the current position $\mathbf{x}^s(\mathbf{X}^s, i\Delta t)$, the material properties in Ω are determined by Eqs. (7) and (8).
- The velocity \mathbf{v}^s on Γ^s is transmitted to the immersed interface Γ^{isi} by Eq. (11) and the velocity boundary condition of $\Gamma^{\nu,\text{isi}}$ is calculated.
- With the known velocity \mathbf{v} and pressure p on Γ^f and Γ^{isi} , the N-S equations are then solved. With the obtained fluid stress $\boldsymbol{\sigma}$, the fluid traction h_i on Γ^{isi} is calculated by Eq. (12).
- End the current time step and begin with step 2 in the next one; or, go on to iterate and remain in the current coupling cycle.

3 Numerical model

3.1 Geometry and grid

A commonly symmetric bi-leaflet structure was employed for the vein model. In the existing studies of the bi-cuspid valve [Bavo, Rocatello, Iannaccone et al. (2016)], the velocity and pressure fields of 3-D and 2-D models were reported to be comparable. Thus,

we presented a 2-D model in this preliminary work to improve research efficiency. Similarly to the work of Soifer et al. [Soifer, Weiss, Marom et al. (2016)], the current 2-D model is a symmetric cross-section of 3-D geometry, and it is also equivalent to an ultrasound view during the evaluation of venous valve performance. Along the longitudinal cross-section of the vein, its central transverse plane is most representative and chosen in the modeling. As shown in Fig. 4, the geometry and scale of this vein model were partly given.

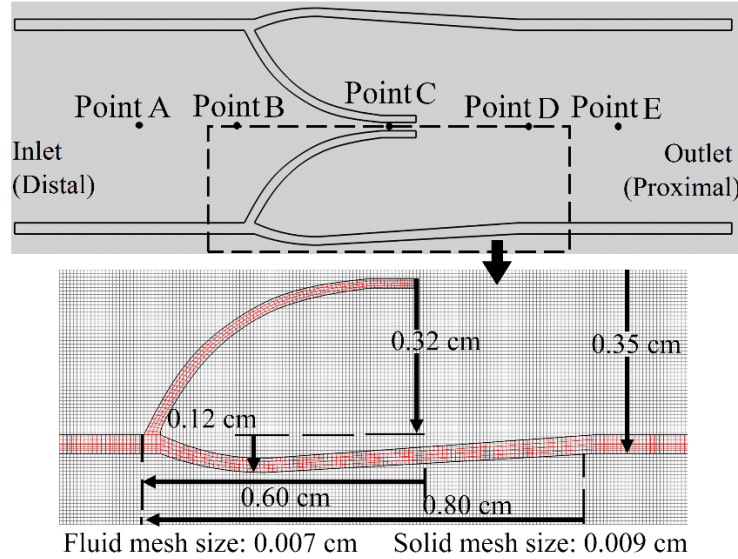


Figure 4: Geometric and finite element models of the vein. Distances of five positions in the longitudinal axis from the inlet are as follows: $x_A=0.45$ cm for point A, $x_B=0.75$ cm for point B, $x_C=1.30$ cm for point C, $x_D=1.80$ cm for point D, $x_E=2.0$ cm for point E

Referring to the geometry of the saphenous vein specimen in Lu et al. [Lu and Huang (2018)], we define the total geometrical parameters which are almost the same as those in our previous vein model [Liu and Liu (2019a)]. The total length of the vein model is 2.5 cm. The Luminal radius is 0.35 mm. In the bulged part of the vein, the distance between the sinus and the exterior is set as 0.12 to approximate the mean diameter 9-10 mm reported in Lu et al. [Lu and Huang (2018)]. The other specification of the anatomy of the vein model is listed in Tab. 1.

Table 1: Detailed parameters of the vein model

Dimension	Size (cm)
Total Length of the vein	2.50
Luminal radius of the vein	0.35
Thickness of the vein wall	0.04

Depth of the leaflet	0.60
Leaflet height (distance between the valve and the wall)	0.32
Average thickness of the distance	0.02
Depth of the sinus	0.80
Sinus height (distance between the leaflet and the sinus)	0.44
Average thickness of the sinus	0.03

According to the viewpoint of the IFEM, the vein was immersed in a channel with length $L=2.4$ cm and height $H=1.1$ cm. This length was carefully set based on the considerations of the anatomical data of the vein and the boundary effect from the inlet and outlet. There are three parts in the vein: (1) the venous wall with length L 2.4 cm, thickness w 0.05 cm, and an outer diameter D 0.7 cm, (2) the venous sinus 0.12 cm high and 0.8 cm deep, and (3) the bi-leaflet valve with height of each leaflet 0.32 cm, depth 0.60 cm and thickness 0.025 cm. The valve base was initially set 1 cm away from the inlet, at the joint of the sinus and the wall. A gap of 0.028 cm was kept between the leaflets for the following adhesive contact calculation. The sinus region also covers the potential contact region similar to that in the real vein. It was noticeable that the distention of the sinus and wall could be included in this channel, which was wider than the vein.

Following the previous research [Liu and Liu (2019a)], the vein was also discretized with a quadrilateral mesh of mean size 0.009 cm, and the channel Ω discretized with a uniform grid of size 0.007 cm. The recommended mesh ratio of (1, 2) [Zhang, Gerstenberger, Wang et al. (2004)] was used for the efficient and effective coupling between the fluid and solid. The employment of the non-body fitted mesh also enabled the finite deformation of the vein, particularly when the valve fluttered. In Fig. 4, five nodal positions of the fluid element along the longitudinal axis were also chosen for analyzing the flow characteristics.

3.2 Materials and boundary conditions

3.2.1 Healthy vein

In biology, a healthy vein was considered elastic. According to the constitutive study of a bovine vein [Lu and Huang (2018)], the valve leaflet could be modeled as hyperelastic material, which was softer than the vessel. Following the biological knowledge of the vessel [Sokolis (2008)], the venous wall applied a linear-elastic constitution. Owing to the scanty information about the venous sinus, it was assumed as the same as that of the wall. Measurements of collagen fiber angle in the similar biological tissues [Humphrey, Strumpf and Yin (1990)] demonstrated that fiber orientation varied regionally and symmetrically about the central radial axis of each leaflet. It reasonably enabled that the material property of the vein model was assumed locally transversely-isotropic.

For the wall and sinus [Buxton and Clarke (2007)], Young's modulus E was set as 2.0 MPa along with Poisson's ratio 0.475 so as to physiologically match their mechanics. Based on the hyperelastic model in Wesly et al. [Wesly, Vaishnav, Fuchs et al. (1975)], a three-parameter type of Mooney-Rivlin constitutive model was adopted, with parameters $c_1=300.0$ kPa, $c_2=40.0$ kPa and $c_3=0$. The constitutions of the vein (wall, sinus and valve) are all detailed in Appendix C.

The blood in the vein is non-Newtonian in physics. When it was at high shear rates ($>100/s$), the blood behaved as close to Newtonian liquid. Following the existing models [Liu and Liu (2006); Zhang, Liu and Khoo (2013)], the material properties of the blood were defined, such as the density ρ^f 1.06 g/cm³ and its dynamic viscosity μ^f 0.036 g/(cm·s) [Kenner (1989)].

In the circulatory system, the venous blood flow exhibits the pulsed and periodical features [Smiseth, Thompson, Lohavanichbutr et al. (1999)]. A periodic velocity condition was then imposed at the distal end of the vein, along with a periodically-varied pressure gradient traversing the vein. A pulsed waveform function for the input condition was chosen to mimic a respiration-dependent flow [Vukicevic et al. (2014)] as shown in Fig. 5.

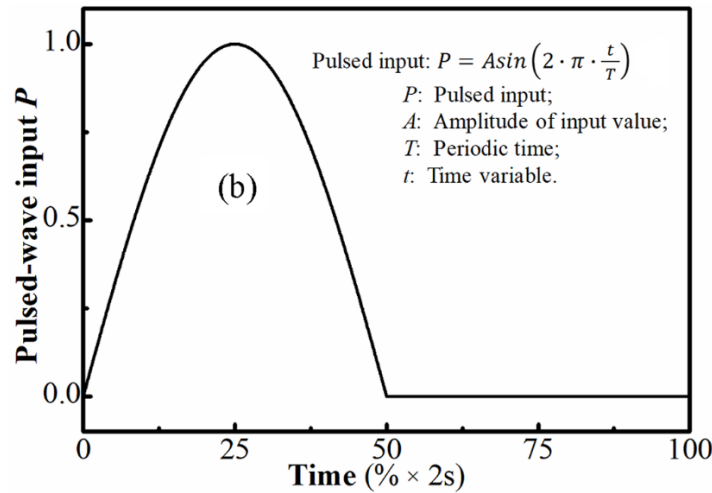


Figure 5: Waveform function of the input velocity and pressure at the inlet

The mathematical formulation of the waveform function is

$$\Psi = \begin{cases} \phi \sin\left(\frac{2\pi t}{T}\right) & , \quad Ti < t < T(i + 0.5) \\ 0 & , \quad T(i + 0.5) < t < T(i + 1) \end{cases} \quad (15)$$

where ϕ is the amplitude of velocity or pressure at the inlet, T is the period of the wave function, and Ti is the i th period of the valve cycle with the integer $i=0, 1, 2, \dots$

Additionally, a weak gravitational acceleration was considered to be consistent with that reported in Lurie et al. [Lurie, Kistner and Eklof (2002)]. Assuming that the fluid is initially stationary. The period T was 2.0 s as the respiration was assumed 30 cycles per min in the healthy vein. The transvascular pressure gradient was $P_{\max}=4.5$ mmHg on the

basis of the physiological publications [Qui, Quijano, Wang et al. (1995); Smiseth, Thompson, Lohavanichbutr et al. (1999)]. Considering that the blood flow was fully developed from the distal end, a parabolic velocity was prescribed for the inflow condition as

$$u_x = V_{\max}y[(D - 2w) - y]/(D - 2w)^2, u_y = 0 \tag{16}$$

where u_x is the velocity in the normal direction of the inlet, u_y the velocity in the tangential direction, y is the coordinate at the inlet, and V_{\max} is the velocity amplitude equaling to 10.0 cm/s. The non-slip condition was prescribed on the top and bottom boundaries of the channel, as well as on the boundaries of the vein. Both ends of the vein were fixed with the x - and y -displacement constraints.

As provided in Appendix B, parameters needed to be known for the solid solution include those in time integration scheme, damping setting and contact algorithm. Following the validated values of the parameters in the solid solver in Liu et al. [Liu and Liu (2019a, 2019b)], the coefficient θ in was set to 0.5, and the damping coefficients $f_m=0.05$ and $f_k=0.272$ were used. For the calculation of the contact force, the potential well ε of -14.0 J was employed, and the equilibrium distance $r_0=0.056$ cm was used. The time-step size in the total computational model was 0.0004 s so that the flow feature of blood crossing single element could be captured and the potential penetration in the contact model could be opposed.

3.2.2 Diseased vein

As reported previously [Eberhardt and Raffetto (2014)], one common etiology of diseased veins was abnormal elastic properties. It prompted us to consider the stiffening or softening of sinus material as the sinus lesions. Therefore, the diseased veins were defined by linearly scaling up or down the elastic modulus of the sinus material [Soifer, Weiss, Marom et al. (2016)]. As listed in Tab. 2, E is 10.0 MPa when the sinus is fibrotic and 400.0 kPa when the sinus is atrophic; for the severe situations, E is 20.0 MPa when the sinus is severely fibrotic and 200.0 kPa when the sinus is severely atrophic. Additionally, the respiration change was also considered and assumed as 60 cycles per min, with the pressure gradient 3.0 mmHg. Then, the other settings of the diseased vein model were the same as those in the assumed healthy vein.

Table 2: Material properties parameters of the diseased vein cases

Diseased sinus	Density (g/cm ³)	Poisson ratio	Yong modulus (MPa)
Severely atrophic	1.10	0.475	0.20
Atrophic	1.10	0.475	0.40
Fibrotic	1.10	0.475	10.0
Severely fibrotic	1.10	0.475	20.0

4 Results and discussion

We simulated the venous valve cycle in 2.0 s in this study. It took 32 hours to complete one simulation in the Intel Core i7-4790HQ processor with the main frequency 3.60 GHz. The simulation was achieved by a single-core and non-parallelized computation was employed. The validity of the mathematical vein model was verified by the benchmark simulation of the healthy vein. The prospective study of the diseased vein was further explored, through the discussion of sinus lesions on the venous valve cycle. The effects of the lesion were then determined by comparing the healthy and the diseased veins.

4.1 Validation of vein model

4.1.1 Valve kinematics

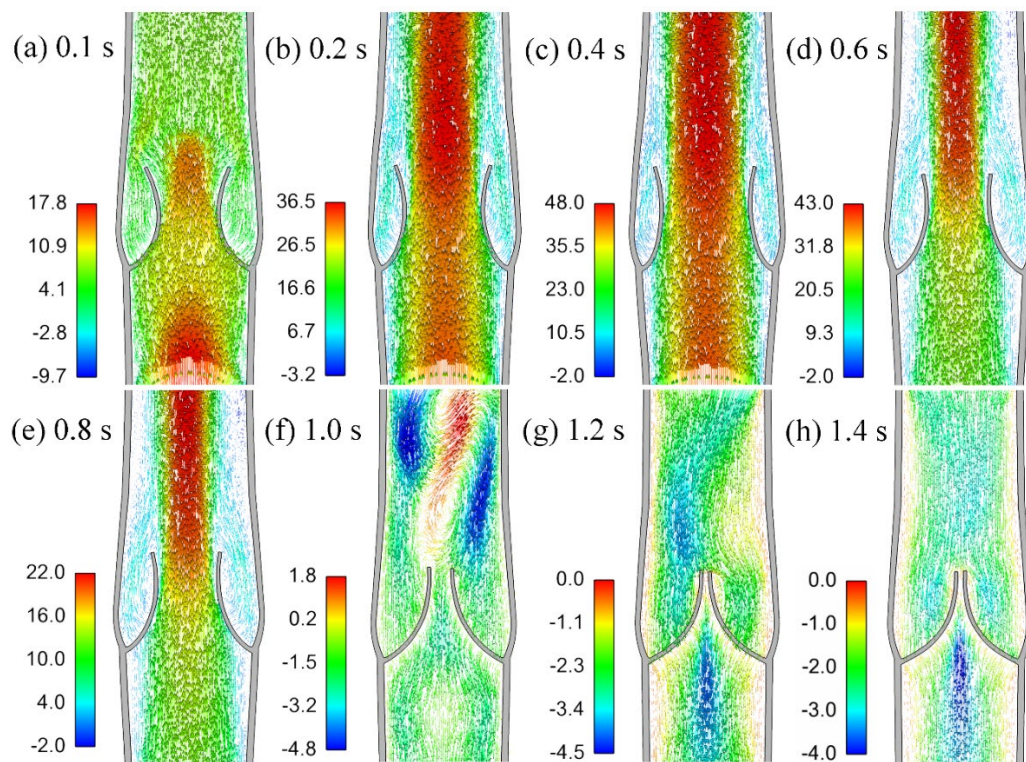


Figure 6: Blood flow (cm/s) and vein deformation during single venous valve cycle. Opening phase: (a) at 0.10 s, (b) at 0.20 s; Equilibrium phase: (c) at 0.40 s; Closing phase: (d) at 0.60 s, (e) at 0.80 s, (f) at 1.00 s, (g) at 1.20 s; Closed phase: (h) at 1.40 s

Figs. 6(a)-6(b) show the periodic behavior of the healthy vein in the opening, equilibrium, closing and closed phases [Zervides and Giannoukas (2013)]. During the initial 0.2 s, the inflowing blood rapidly flowed into the lumen and pushed the valve, the leaflets rotated immediately and the opening orifice between the leaflets increased. A core flow downstream became fully developed, as shown in Fig. 6(b). Subsequently, the opening orifice size reached the maximum level. The valve leaflets entered into an equilibrium state, and fluttered as the blood streamed past. At around 0.6 s, the pressure gradient of

the inflow was decreasing, the valve began to close while the reversed flow was formed at the outlet [Buescher, Nachiappan, Brumbaugh et al. (2005)], as shown in Figs. 6(d)-6(g). After about 1.2 s, the semi-lunar leaflets were completely closed, and minor changes were seen in fluid velocity and solid deformation. In the closed phase, the adhesive contact force opposed the penetration between the leaflets, and the leaflets closed and had less fluctuation which could be neglected (see Fig. 7). The velocity of the venous flow upon the leaflet surface was 0 cm/s in Fig. 6(h) owing to the non-slip condition. And it was seen that the venous blood flowed reversely owing to the gravity, and the corresponding value was non-zero. In this single cycle, the non-slip boundary conditions were satisfied in the FSI computation, and the deformation of the sinus and blood vessels was less significant relative to the valve.

Comparing to the results for the healthy vein case in previous research [Liu and Liu (2019a)], the leaflet deformation in this paper were different, which is owing to the different settings of the elastic model of the vein, the pulsed inflowing conditions and the period time. Similarly, the results in the following sections were also consequently different.

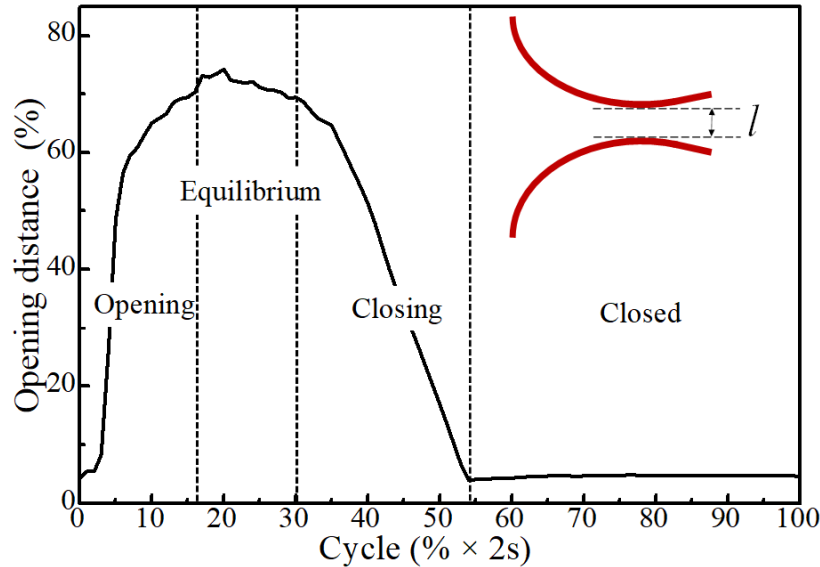


Figure 7: Time variation of the orifice size

Table 3: Maximum effective orifice size of the vein

Case	Orifice size (% of the diameter)
Calculated result	74.2%
Physiological range [Lurie and Kistner (2012)]	60%-70%

The time period of each phase in the valve cycle could be clearly distinguished by the variation of the opening orifice, as shown in Fig. 7. In the equilibrium phase, it was seen

that the variation of the effective orifice size was rough, which should be induced by the obvious change of the inflowing velocity. As such rough variation was small, it should be insignificant when there might be numerical artefacts. The maximum effective orifice size was 0.503 cm, which is 74.2% of the diameter. Although this is an idealized 2-D venous model, its deformation agrees with the real situation and is close to the physiological range 60%-70% (in the human saphenous vein [Lurie and Kistner (2012)], as shown in Tab. 3. In other words, the calculated venous deformation had a good agreement with that in physiology, and the proposed FSI model was verified. It indicated that this model could be effectively used for further analysis of the valve cycle in the vein under other physiological situations.

4.1.2 Blood kinematics

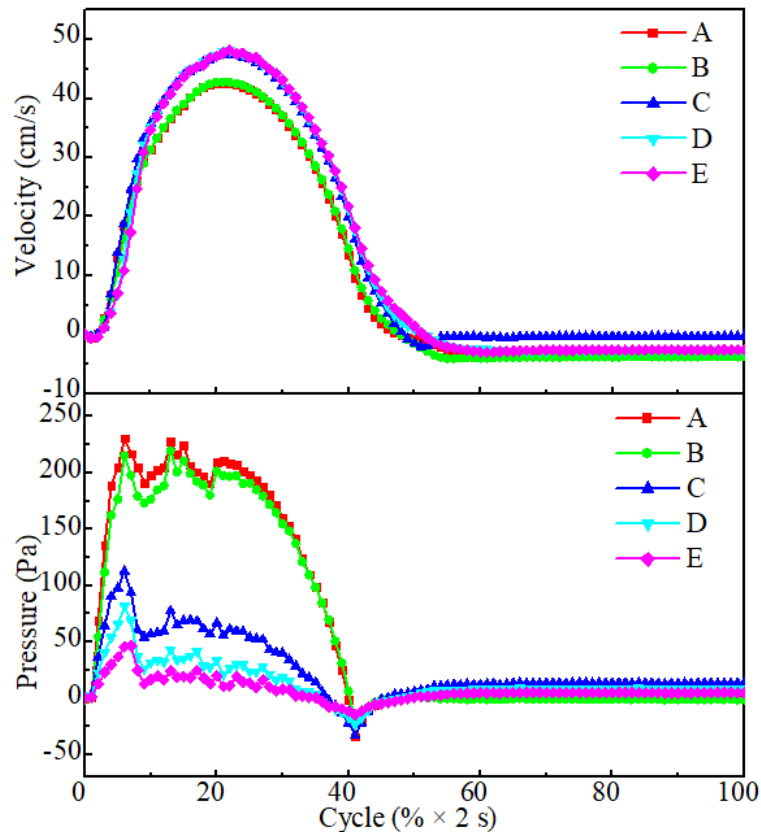


Figure 8: Fluid dynamic characteristics of venous blood along the longitudinal axis. Time variations of (a) fluid velocity and (b) pressure

Fig. 8 displays time-dependent variations in blood velocities and pressures at five points (which are shown in Fig. 4) along the longitudinal axis of the vein. The velocities and pressures at different positions were influenced by the inflow conditions and the reversed flow was induced by gravity. When the valve was closing at 0.6 s-1.0 s, there was a distinct transition of flow direction from x to $-x$ -direction. The valve blocked the

inflowing blood and the ejection was formed for mass conservation. Fig. 8(a) also shows that the velocity value in the proximal lumen (Point D or Point E) was higher than that of the distal (Point A or Point B). Fig. 8(b) shows there is a pressure drop from the distal to the proximal in the opening and equilibrium periods.

In this paper, the blood was assumed incompressible liquid. As is known that in the fluid mechanics, the Reynolds number R_e and the Womersley number α are expressed as

$$R_e = \rho v d_h / \mu \quad (17)$$

$$\alpha = R(\omega \rho / \mu)^{1/2} \quad (18)$$

where d_h is the hydraulic diameter in a tube, R is the radius, ω is the angular frequency of the oscillation (or $2\pi/T$).

Taking the velocities (see Fig. 8(a)) at the five positions of Points A-E (see Fig. 4), we calculated the Reynolds number at those positions, and the maximum pressure was 1137 Pa at Point D while the value at the orifice was 700 Pa at Point C. Therefore, the transvalvular flow was still featured below the bound of the turbulent flow. Similarly, the Womersley numbers were calculated and the maximal value was 3.8 Pa at Point D. The maximum value at the orifice was 2.38 Pa at Point C. Thus, the waveform profile of this flow was compatible to that (2.77-16.6) in the human vein (about 0.5-3.0 cm in diameter) [Whitmore (1968)].

As the variation of the orifice size and the velocities in the equilibrium period was small, the flow could be regarded as approximately steady-state. Meantime, the five positions of Point A-E at the same streamline. According to the principle of energy conservation in the pipe flow, the velocities and pressures of Point A-E should satisfy the generalized Bernoulli's equation

$$p_I + \rho v_I^2 / 2 + \rho g_x x_I = p_J + \rho v_J^2 / 2 + \rho g_x x_J + h_{IJ}, \quad (19)$$

Where p_I and p_J are the hydrostatic pressures at Point I and Point J, respectively, while I, J=A-E; g_x is the acceleration in x -direction and equaling to $-0.1g$, g is the gravitational acceleration; x_I and x_J are the distances from the inlet to Point I and Point J, respectively; h_{IJ} is the other energy loss (per volume) when flowing from Point I to Point J.

With regards to Point A and Point B, taking their velocities and pressures at 0.4 s into Eq. (19), then $p_A - p_B + \rho g_x (x_A - x_B) = 3.0$ Pa and $\rho v_B^2 / 2 - \rho v_A^2 / 2 = 0.5$ Pa, thus $h_{AB} = 2.5$ Pa. As the diameters of their cross-sections were almost the same, this small energy loss could be attributed to the internal friction (or viscosity). However, when considering Point B and Point C, $p_B - p_C + \rho g_x (x_B - x_C) = 126.9$ Pa and $\rho v_B^2 / 2 - \rho v_C^2 / 2 = 20.9$ Pa, thus $h_{AB} = 106.0$ Pa which was far beyond the order of the energy loss induced by the viscosity. Combining with the blockage from the valves, it could be deduced that the valves induced the blockage of the inflow and led to the strong fluid resistance, which made apparent work and consumed the kinetic energy of the blood flow from the proximal to the distal. Thus, the fluid resistance from the valve blockage should be also significant in leading to the pressure drop.

Additionally, we chose the moment 0.42 s when the velocities at the five positions were at the peak. As shown in Tab. 4, the maximum value of $\rho v_I^2 / 2 - \rho v_J^2 / 2$ was 12.3 Pa

between Point A and Point E, while the maximum value of the transvalvular pressure gradient was 189.5 Pa, and the maximum value of $\rho g_x(x_E - x_A)$ was 16.0 Pa. Between Points B and D, the transvalvular pressure difference fluctuated and was 160-190 Pa at the stable state, which was 1.22-1.45 mmHg. The pressure gradient is close to the range of 1.0-5.0 mmHg in the saphenous vein [Tien, Chen, Berwick et al. (2014b)] when the maximum orifice is detected. The consistency of the pressure values further indicates the validity of the flow model.

Table 4: The peak velocities at the five positions along the longitudinal axis and the corresponding pressure at the same moment

Point	A	B	C	D	E
Velocity (cm/s)	42.5	42.8	47.4	48.2	48.1
Pressure (Pa)	208.7	196.8	61.2	29.5	19.2

As shown in Fig. 9, we found that the 2-D flow pattern in the orifice was parabolic and could be fully-developed with the agreement of the Womersley number. Considering the special feature of velocity distribution in its arbitrary middle plane of the pipe flow, it is reasonably assumed that the velocities of the vein should be also elliptically distributed in the cross-section of its “3D model”.

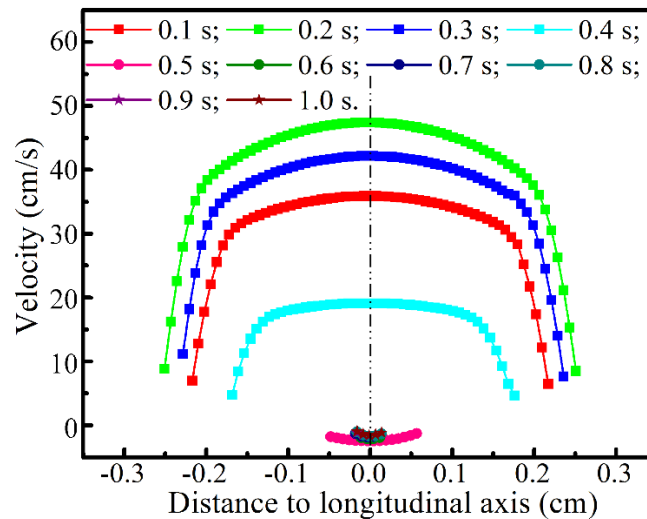


Figure 9: Parabolic flow pattern at the orifice at the different instants of times

As is mentioned that the velocity results involve symmetrical expansion of the model outputs, the blood flow rate could be calculated with the orifice size. And the mean velocity \bar{v} at Point C equals to 36.84 cm/s by solving

$$\bar{v} = Q/A = [0.5\pi l_{\text{sinus}} \int_0^{l_{\text{GOA}}} v^f dy] / (0.25\pi l_{\text{sinus}} l_{\text{GOA}}), \quad (20)$$

where Q is the venous volume flow rate [Qui, Quijano, Wang et al. (1995)], A is the geometric orifice area (GOA) [Konig, Mcallister, Dusserre et al. (2009)]. It should be noted the orifice was reported as an elliptically-shaped cross-section, the distension of the sinus l_{sinus} is the short axis, and the orifice size l_{GOA} is the long axis. Also, the result was within the range of experimental mean flow rate [Kenner (1989)] (Tab. 5), which validated the efficacy of the mathematical model.

Compared to real venous flow, there were some differences in our model due to its simplicity. Particularly when the waveforms of velocity and pressure were assumed regular, which approximated to that of the positive semi-sine. The eddy characteristics in the 2-D flow were more straightforward than that in the 3-D flow, especially for the helical flow [Chen, Berwick, Krieger et al. (2014); Chen, Diaz, Fedor et al. (2018)] which would have a more evident discrepancy in details. Nevertheless, these simplifications also facilitate the implementations. The flow problem within the complex boundary was solved. Along with the periodic rotation of the valve, the venous blood flowed upstream and downstream repeatedly in the proposed cycles of the model.

Table 5: The mean blood flow velocity of the vein

Case	Mean flow velocity (cm/s)
Calculated result	36.84
Experimental range [Moneta, Bedford, Beach et al. (1988)]	15.0-40.0

4.1.3 Valve and blood dynamics

The fluid pressure and structural dynamic response of the venous root region were the most significant due to the material gradients at that site, as shown in Figs. 10(a)-10(b). At the leading edge of the valve root, the peak first principal stress (FPS) was 8.88 kPa and the corresponding transvalvular pressure gradient was 125 Pa, suggesting that the imposition of this hydrodynamic action was associated with the blockage from the valve. It indicated that the root of the valve was an environmentally sensitive region of the vein, and was in line with the knowledge in physiology [Meissner, Moneta, Burnand et al. (2007); Davies (2007)].

Furthermore, the fluid wall shear stress (FWSS) was maximum (3.36 Pa) at the upper edge of the valve and minimum (approximately 0.70 Pa) at the base region of the sinus side of the leaflet, which was consistent with the experimental and mathematical results (0.4 Pa-4.0 Pa) published in Papaioannou et al. [Papaioannou, Karatzis, Vavuranakis et al. (2006); Ariane, Wen, Vigolo et al. (2017)]. The solid wall shear stress (SWSS) was maximum on the back of the valve root and reached 16.5 kPa, also consistent with that in the existing stress level (5 kPa-30 kPa) [Chen, Berwick, Krieger et al. (2014); Whitmore (1968)]. These results corroborated the previous finding that the vascular epithelial cells on the base region of the valve were sensitive to fluid shear stress [Simmons, Grant, Manduchi et al. (2005)]. With rather small fluid shear stress, there would be significant solid stress upon the valve. It could further explain that any disturbance in the

physiological balance of the environment would induce mechanotransduction and result in the release of white blood cells [Davies (2007)]. As was reported that these cells adhere to the surface and accumulate, leading to an inflammatory reaction that deteriorates the venous integrity. So, the analysis of the WSS was available when the presented model was employed to mimic the venous physiology.

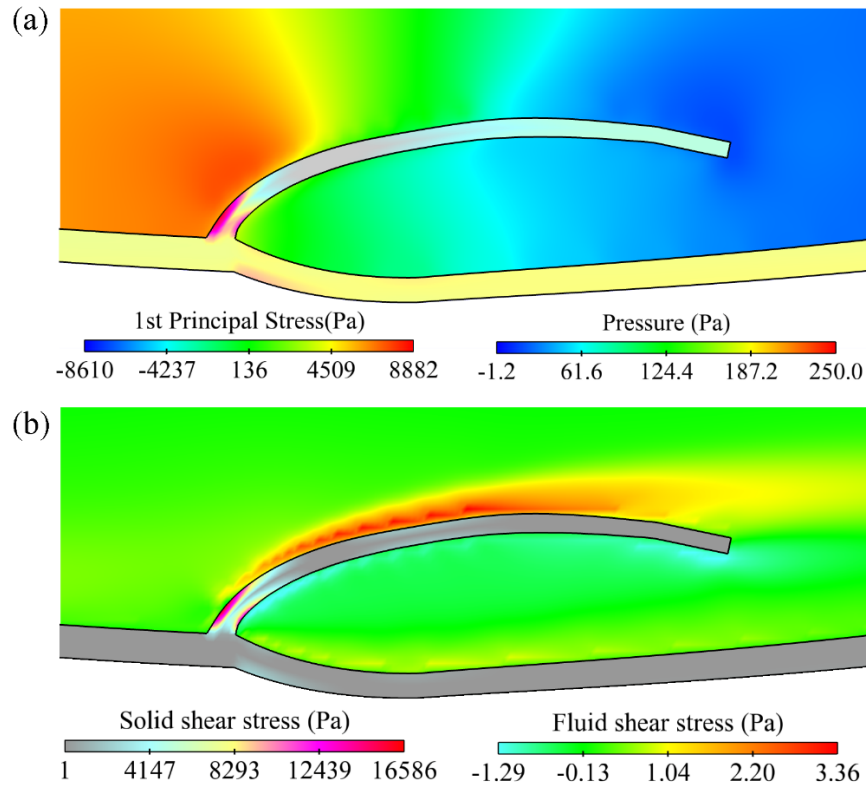


Figure 10: (a) The first principal stress and the corresponding blood pressure, (b) The maximum SWSS and the corresponding FWSS

4.2 Comparisons between healthy and diseased cases

4.2.1 Effects of sinus lesions on valve and blood kinematics

For the kinematics of the vein, the opening-closing behavior of venous valves and their fluid dynamics are given, such as the orifice size, the transvalvular pressure gradient, and the transvalvular flow rate.

As shown in Fig. 11, the valve deformation exhibited sensitivity to the assumed sinus lesion. The opening magnitude of the orifice between the leaflets was inversely proportional to the elastic modulus of the sinus. Instead, the duration of the equilibrium phase was proportional to the elastic modulus of the sinus. When the sinus was atrophic, the GOA of the vein increased by 20%, particularly when the situation was severe it increased by 31.6%. When the sinus was fibrotic, the decrease in the GOA was 9.8%-11.4%, and it differed slightly regardless of the severe situation or not. It indicated that

the vein deformation was more sensitive to the atrophic lesion. The maximum orifice diameter was reduced by 3.3% in the fibrotic case and increased by 12.1% in the atrophic case relative to the healthy vein (Tab. 6). Therefore, it is important to consider the flexibility of the venous sinus structure when modeling the vein, especially when the latter is diseased. When the mechanical properties of the venous sinus are disrupted, sinus expansion and contraction would have a significant effect on the valve deformation.

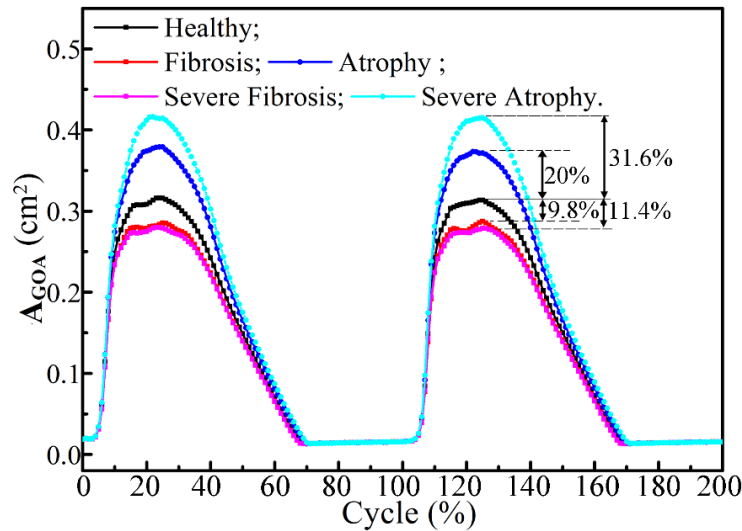


Figure 11: Geometric orifice areas of the vein for different cases

Table 6: The maximum orifice sizes in different vein models

Case	Orifice area (cm ²)	Ratio of orifice to diameter (%)
Healthy one	0.316	66.35%
Sinus with fibrosis	0.285	61.50%
Sinus with atrophy	0.379	75.24%
Sinus with severe fibrosis	0.279	60.40%
Sinus with severe atrophy	0.416	80.40%

Corresponding to the abnormal deformation of the vein, the blood flow also became abnormal, as shown in Fig. 12. The maximum hydrodynamic pressure imposed on the leaflet occurred earlier when the sinus was softer. The pressure gradients near the valves increased by 13.5% and 15.9% in the fibrotic cases; it decreased by 8.7% and 12.7% in the atrophic case. It showed that the pressure gradient in the diseased vein with the severe lesion (fibrosis/atrophy) was close to the one in the mild situation. Taken together, the vascular motion was significantly affected by the orifice size and transvalvular pressure

gradient. Similarly to the valve lesion [Soifer, Weiss, Marom et al. (2016)], the normal valve functioning was also influenced by the sinus lesions.

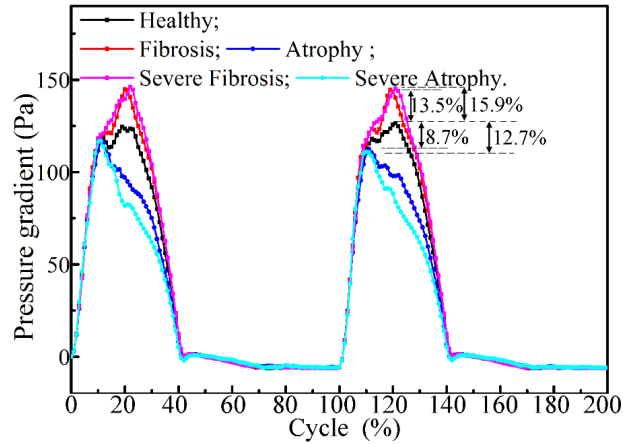


Figure 12: Transvalvular pressure gradient (between Point B and Point D) of the vein for different cases

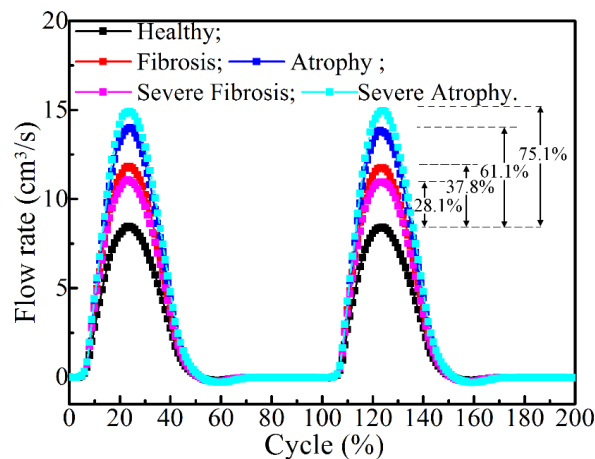


Figure 13: Transvalvular flow rate (between Point B and Point D) of the vein for different cases

Using Eq. (18) in Section 4.1.2, the flow rate was calculated. Fig. 13 shows that the flow rate across the valves increased after the sinus became abnormal. The flow rate increased by 28.1% for fibrotic lesions and severe fibrosis, and it increased by 61.1% for atrophic lesion and severe atrophy. It was mentioned that the flow rate Q is related to the GOA and the velocity pattern at the orifice. Combined with that the decrease in the GOA was induced by the fibrotic sinus lesion, it could be deduced the velocity of the ejection flow sharply increased and the shear rate was even much higher. It indicated that the atrophic lesion might increase the risk of suffering from stronger fluid action or even damage. For example, there would be a more significant increase in the flow rate and it might cause

vasospasm, if the atrophic sinus was found at a cerebral vein. In addition, a significant increase of the venous flow might negatively influence the flow rate of the neighboring veins [Soifer, Weiss, Marom et al. (2016)]. However, this described mechanism indicated that the assumed sinus lesion did not lead to the incompetence of the valve. And the transportation of blood could be improved properly when the sinus of a prosthetic valve was designed to be soft, such as the modulus was scaled down less than 5.0 times.

4.2.2 Effects of sinus lesions on valve and blood dynamics

Fig. 14 plotted the FPS, the pressure, the SWSS and FWSS in different vein models when the opening orifice was maximum. Under the different situations, almost all the peak FPS and SWSS of the vein occurred at the forward side of the root of the valve. Meantime, the pressure gradient imposed at the root of the valve was still maximum. It indicated that the sensitive position of the vein remained the same when it suffered from the sinus lesions.

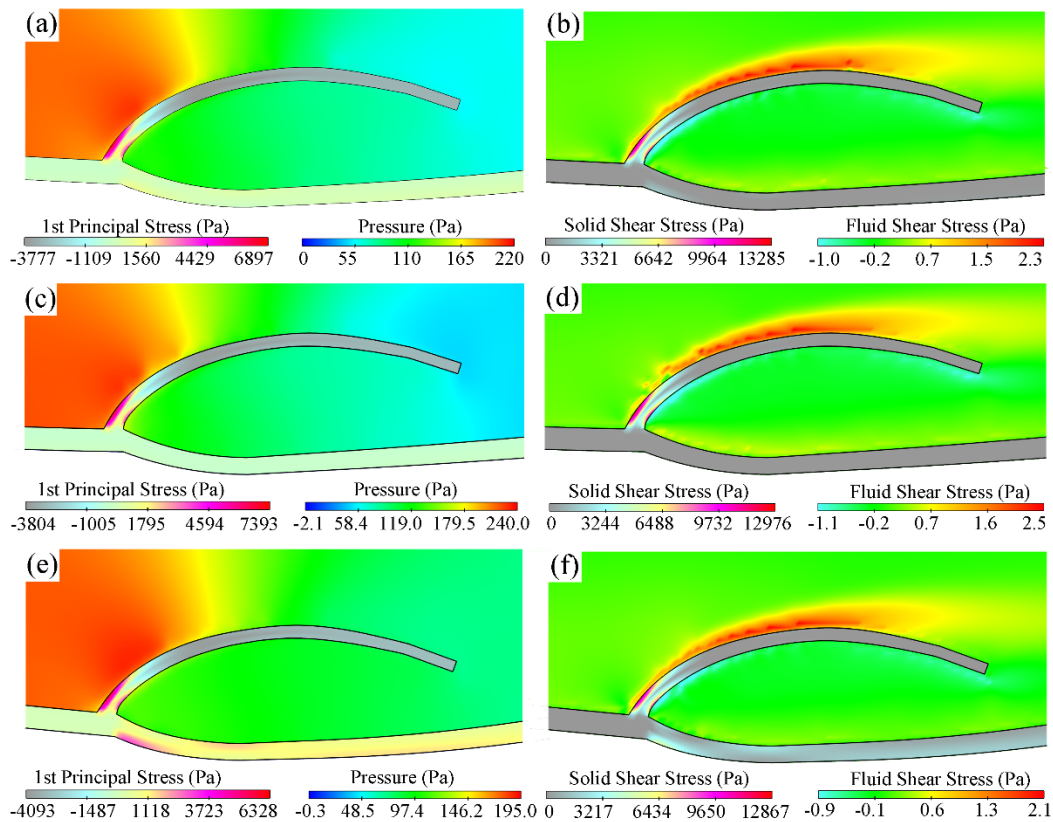


Figure 14: First principal stress and pressure in (a) the healthy vein, (c) the diseased vein with fibrotic sinus and (e) the diseased vein with atrophic sinus at the maximum opening orifice. The corresponding solid shear stress and fluid shear stress in (b) the healthy vein, (d) the diseased vein with fibrotic sinus and (f) the diseased vein with atrophic sinus

Additionally, the fluid shear stresses at the base region of the sinus side of the leaflet were small (below 1.0 Pa), due to the lowest shear rate. The maximum FWSS appeared

on the upper edge of the leaflet. Those results were similar to those in the diseased veins with valve lesion [Soifer, Weiss, Marom et al. (2016)]. An evident discrepancy between them was the increase in the FPS/SWSS at the exterior wall of the sinus if the sinus was atrophic, as shown in Figs. 14(e) and 14(f).

The variation of the leaflet shear stress exhibited a proportional relationship with that of the sinus modulus which further agreed with that for the diseased vein with valve lesion [Soifer, Weiss, Marom et al. (2016)]. To be clearer, we presented the time-variation of the SWSS on the valve root along with the neighboring FWSS, as shown in Figs. 15 and 16.

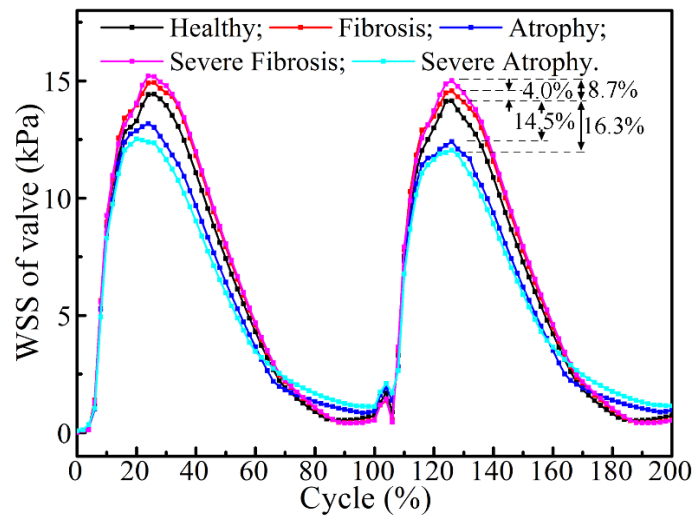


Figure 15: Effects of sinus lesions on the solid wall shear stress (SWSS) on the valve root

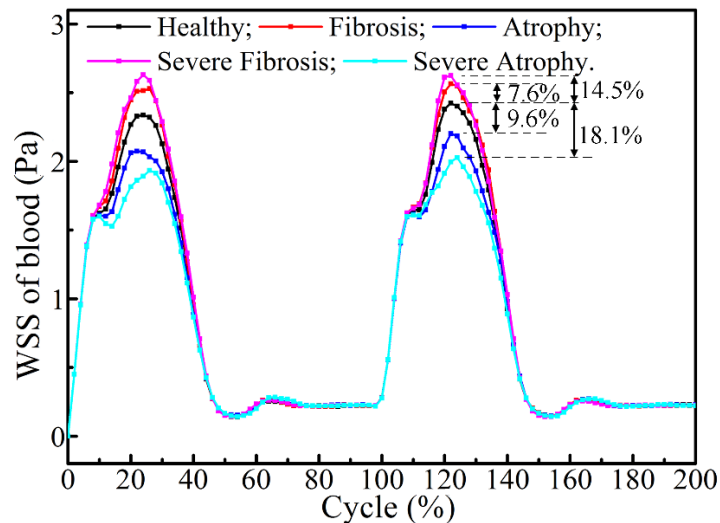


Figure 16: Effects of sinus lesions on the fluid wall shear stress (FWSS) near the valve root

The law of the SWSS for different vein models was the same in different cycles. The SWSS increased with the elastic modulus of the sinus increasing, although the difference of the SWSS between fibrosis and severe fibrosis or between atrophy and severe atrophy was unapparent. It indicated the effect of scaling up or down the sinus modulus was limited to a certain level (5.0 times), and the leaflet response could be less sensitive to such further variation.

Owing to the rapid behavior of the opening, the increase of SWSS in the opening phase was more apparent than that in the closing or closed phase. Compared to the fibrosis of the sinus, the difference between the diseased vein and the healthy vein was more significant induced by the atrophy. Such increases for the fibrotic case were 4.0% and 8.7%, while the decreases for the atrophic cases were 14.5% and 16.3%. Similarly, the increases of the FWSS for the fibrotic case were 7.6% and 14.5%, and more significant than the decreases of 9.6% and 18.1% for the atrophic cases. Such a law of the variation of shear stress owing to the venous lesion was similar to that in the previous reports [Soifer, Weiss, Marom et al. (2016)], we surmised that the atrophic lesion had an apparent effect on the mechanical response.

The major mechanism of FWSS influencing on valve biology is that the low shear stress regions at the pockets behind the leaflets. For both healthy and diseased veins, this may cause flow stagnation and low FWSS. According to Fig. 16, the FWSS became lower with the decrease of the sinus. In pathology, it decreased the atheroprotective and anti-inflammatory factors because endothelium and glycocalyx are known to sense the FWSS and initiate mechanotransduction. At the sinus region, the adhesion of inflammatory and thrombotic cells then increased, and the deposition or permeation of these cells onto the vessel wall was enhanced. Owing to the material gradient at the base of the valve, the SWSS act on the surfaces of leaflets and vessel walls was significant. For evaluation of the valve functioning, a following mechanical cost [Soifer, Weiss, Marom et al. (2016)] was usually defined to quantitatively analyze the effect,

$$\text{Cost function} = \text{Solid WSS} / \text{Fluid WSS}, \quad (19)$$

Combined with the resulting FWSS with SWSS, the maximum mechanical cost of the vein occurred at 0.5 s or 1.5 s. At this time, the FWSS at the sinus side of the valve root was 0.10 Pa, agreed well with that in Chen et al. [Chen, Berwick, Krieger et al. (2014)]. Accordingly, the mechanical cost of the healthy vein was 5.5×10^4 . The apparent difference of the cost was normalized as a ratio of 1: 0.87: 1.08: 0.64: 1.23 for the healthy vein, the diseased veins with sinus lesions of fibrosis and atrophy, and those with severe fibrosis and atrophy. The hypothesized mechanism suggested an upper limit, although softer sinus in prosthetic valve facilitated blood transportation. Due to the sensitivity to mechanical stimuli, white blood cell accumulation and adsorption on the vascular surface would damage the elasticity of venous material [Davies (2007)]. We deduced therefore that atrophic lesion of the sinus was supposed to improve the sensitivity of the diseased vein to fluid shear stress, and the risk of damage to the venous endothelial cells was increased when the sinus was subjected to the same magnitude of FWSS.

5 Conclusions

An FSI model of the vein was established using the modified IFEM and the adhesive contact algorithm. Both the fluid-structure and solid-solid interactions were included in the model. The fibrosis and atrophy of sinus were studied as vein lesions. And the valve opening orifice size, blood flow rate and wall shear stress were quantitatively analyzed. The primary conclusions were given as below:

- The proposed FSI method was available in capturing the interaction between the blood and the vein. The contact force opposed further penetration between leaflets when the valve was closed. The periodic fluttering of the leaflet, and the periodic forward and reversed flows were reproducible.
- The validity of the presented mathematical model was verified by related experimental and theoretical findings of the healthy vein. The accuracies of the valve and blood dynamics in the 2-D model were sufficient for analysis of the vein under normal/abnormal physiological conditions along its central transverse plane.
- Variation of the valve movement was inversely proportional to the elastic modulus of the sinus, $A_{GOA}(\text{Severe atrophy}) > A_{GOA}(\text{Atrophy}) > A_{GOA}(\text{Healthy}) > A_{GOA}(\text{Fibrosis}) > A_{GOA}(\text{Severe fibrosis})$. Instead, the transvalvular pressure gradient increased with the elastic modulus of the sinus increasing. However, the effects of both were limited when the modulus was scaled to a certain level, and never caused the incompetence of the valve.
- Either the stiffening or the softening of the sinus led to an increase in the blood flow rate. Such an increase was not always beneficial when a prosthesis was designed, as the overloading of the cardiovascular system may develop into cardiac failure.
- The sinus region was the possible position of the tissue failure, since low blood WSS and the highest leaflet WSS were seen at that site. Relative to the fibrotic lesion, the atrophic lesion resulted in a greater increase in shear stress along with significant SWSS on the sinus surface.
- Compared to the healthy vein, an increase of mechanical cost in the diseased vein with atrophic sinus showed increased sensitivity to mechanical stimuli.

The presented results were still partly understood although the FSI model was valid. And the understandings could be complete only if the related biological knowledge was clearly known. Additionally, there was still room in this research, such as the 3-D model, the helical flow, and more realistic structure. And this code was also under private development to improve its current shortcomings. We will devote ourselves to those improvements so that the employment of the present study could be more useful in the prosthesis design of vein, as well as the code could be open-sourced in the future work.

Acknowledgement: The work is partially funded by Key Aviation Scientific and Technological Laboratory of High-speed Hydrodynamic under grant MJ-2015-F-028.

Conflicts of Interest: The authors declare that they have no conflicts of interest to report regarding the present study.

References

- Aluri, S.; Chandran, K. B.** (2001): Numerical simulation of mechanical mitral heart valve closure. *Annals of Biomedical Engineering*, vol. 29, no. 8, pp. 665-676.
- Ariane, M.; Wen, W.; Vigolo, D.; Brill, A.; Nash, F. G. B. et al.** (2017): Modelling and simulation of flow and agglomeration in deep veins valves using discrete multi physics. *Computers in Biology and Medicine*, vol. 89, no. 5, pp. 96-103.
- Bavo, A. M.; Rocatello, G.; Iannaccone, F.; Degroote, J.; Vierendeels, J. et al.** (2016): Fluid-structure interaction simulation of prosthetic aortic valves: comparison between immersed boundary and arbitrary Lagrangian-Eulerian techniques for the mesh representation. *PLoS One*, vol. 11, no. 4, pp. e0154517.
- Buescher, C. D.; Nachiappan, B.; Brumbaugh, J. M.; Hoo, K. A.; Janssen, H. F.** (2005): Experimental studies of the effects of abnormal venous valves on fluid flow. *Biotechnology Progress*, vol. 21, no. 3, pp. 938-945.
- Buxton, G. A.; Clarke, N.** (2007): Computational phlebology: the simulation of a vein valve. *Journal of Biological Physics*, vol. 32, no. 6, pp. 507-521.
- Carpentier, P. H.; Maricq, H. R.; Biro, C.; Claire, O. P.; Franco, A.** (2004): Prevalence, risk factors, and clinical patterns of chronic venous disorders of lower limbs: a population-based study in france. *Journal of Vascular Surgery*, vol. 40, no. 4, pp. 650-659.
- Chen, H. Y.; Berwick, Z.; Krieger, J.; Chambers, S.; Lurie, F. et al.** (2014): Biomechanical comparison between mono-, bi-, and tricuspid valve architectures. *Journal of Vascular Surgery-Venous and Lymphatic Disorders*, vol. 2, no. 2, pp. 188-193.
- Chen, H. Y.; Diaz, J. A.; Fedor, L.; Chambers, S. D.; Kassab, G. S.** (2018): Hemodynamics of venous valve pairing and implications on helical flow. *Journal of Vascular Surgery: Venous and Lymphatic Disorders*, vol. 6, no. 4, pp. 517-522.e1.
- Cheng, J.; Yu, F.; Zhang, T. L.** (2019): OpenIFEM : a high performance modular open-source software of the immersed finite element method for fluid-structure interactions. *Computer Modeling in Engineering & Sciences*, vol. 119, no. 1, pp. 91-124.
- Coffman, J. D.; Lempert, J. A.** (1975): Venous flow velocity, venous volume and arterial blood flow. *Circulation*, vol. 52, no. 1, pp. 141-45.
- Davies, P. F.** (2007): Endothelial mechanisms of flow-mediated athero-protection and susceptibility. *Circulation Research*, vol. 101, pp. 10-12.
- Dydek, E. V.; Chaikof, E. L.** (2015): Simulated thrombin responses in venous valves. *Journal of Vascular Surgery: Venous and Lymphatic Disorders*, vol. 4, no. 3, pp. 329-335.
- Eberhardt, R. T.; Raffetto, J. D.** (2014): Chronic venous insufficiency. *Circulation*, vol. 130, no. 4, pp. 333-346.
- Fan, H.; Ren, B.; Li, S.** (2015). An adhesive contact mechanics formulation based on atomistically induced surface traction. *Journal of Computational Physics*, vol. 302, no. 1, pp. 420-438.
- Fedkiw, R. P.; Aslam, T.; Merriman, B.; Osher, S.** (1999): A non-oscillatory Eulerian approach to interfaces in multimaterial flows (the Ghost Fluid Method). *Journal of Computational Physics*, vol. 152, no. 2, pp. 457-492.

- Hertzberg, B. S.; Kliever, M. A.; Delong, D. M.; Lalouche, K. J.; Paulson, E. K. et al.** (1997): Sonographic assessment of lower limb vein diameters for implications for the diagnosis and characterization of deep venous thrombosis. *American Journal of Roentgenology*, vol. 168, no. 5, pp. 1253-1257.
- Hudgins, P. A.** (2003): Imaging of the cavernous sinus. *Techniques in Neurosurgery*, vol. 8, no. 4, pp. 211-219.
- Humphrey, J. D.; Strumpf, R. K.; Yin, F. C.** (1990): Determination of a constitutive relation for passive myocardium: I. a new functional form. *Journal of Biomechanical Engineering*, vol. 112, no. 3, pp. 333-339.
- Kenner, T.** (1989): The measurement of blood density and its meaning. *Basic Research in Cardiology*, vol. 84, no. 2, pp. 111-124.
- Konig, G.; Mcallister, T. N.; Dusserre, N.; Garrido, S. A.; Iyican, C. et al.** (2009): Mechanical properties of completely autologous human tissue engineered blood vessels compared to human saphenous vein and mammary artery. *Biomaterials*, vol. 30, no. 8, pp. 1542-1550.
- Korchi, A. M.; Cuvinciuc, V.; Caetano, J.; Becker, M.; Lovblad, K. O. et al.** (2014): Imaging of the cavernous sinus lesions. *Diagnostic and Interventional Imaging*, vol. 95, no. 9, pp. 849-859.
- Li, C.; Baird, C.; Yao, J.; Yang, C.; Wang, L.** (2019): Computational modeling of human bicuspid pulmonary valve dynamic deformation in patients with tetralogy of fallot. *Computer Modeling in Engineering & Sciences*, vol. 119, no. 1, pp. 227-244.
- Li, Z.; Wang, X. S.** (2019): Preface : simulation of fluid-structure interaction problems. *Computer Modeling in Engineering & Sciences*, vol. 119, no. 1, pp. 1-3.
- Liu, X.; Liu, L.** (2019): An immersed transitional interface finite element method for fluid interacting with rigid/deformable solid. *Engineering Applications of Computational Fluid Mechanics*, vol. 13, no. 1, pp. 337-358.
- Liu, X.; Liu, L.** (2019): Effect of valve lesion on venous valve cycle: a modified immersed finite element modeling. *PLoS One*, vol. 14, no. 3, pp. e0213012.
- Liu, Y.; Liu, W.** (2006): Rheology of red blood cell aggregation by computer simulation. *Journal of Computational Physics*, vol. 220, no. 1, pp. 139-154.
- Lu, J.; Huang, H.** (2018): Biaxial mechanical behavior of bovine saphenous venous valve leaflets. *Journal of the Mechanical Behavior of Biomedical Materials*, vol. 77, no. 1, pp. 594-599.
- Lurie, F.; Kistner, R. L.** (2012): The relative position of paired valves at venous junctions suggests their role in modulating three-dimensional flow pattern in veins. *European Journal of Vascular and Endovascular Surgery*, vol. 44, no. 3, pp. 337-340.
- Lurie, F.; Kistner, R. L.; Eklof, B.** (2002): The mechanism of venous valve closure in normal physiologic conditions. *Journal of Vascular Surgery*, vol. 35, no. 4, pp. 713-717.
- Lurie, F.; Kistner, R. L.; Eklof, B.; Kessler, D.** (2003): Mechanism of venous valve closure and role of the valve in circulation: a new concept. *Journal of Vascular Surgery*, vol. 38, no. 5, pp. 955-961.

- McLafferty, R. B.; Passman, M. A.; Caprini, J. A.; Rooke, T. W.; Markwell, S. A. et al.** (2008): Increasing awareness about venous disease: the american venous forum expands the national venous screening program. *Journal of Vascular Surgery*, vol. 48, no. 2, pp. 394-399.
- Meissner, M. H.; Moneta, G.; Burnand, K.; Gloviczki, P.; Lohr, J. M. et al.** (2007): The hemodynamics and diagnosis of venous disease. *Journal of Vascular Surgery*, vol. 46, no. 6, pp. 4S-24S.
- Moneta, G. L.; Bedford, G.; Beach, K.; Strandness, D. E.** (1988): Duplex ultrasound assessment of venous diameters, peak velocities, and flow patterns. *Journal of Vascular Surgery*, vol. 8, no. 3, pp. 286-291.
- Papaioannou, T. G.; Karatzis, E. N.; Vavuranakis, M.; Lekakis, J. P.; Stefanadis, C.** (2006): Assessment of vascular wall shear stress and implications for atherosclerotic disease. *International Journal of Cardiology*, vol. 113, no.1, pp. 1-18.
- Qui, Y.; Quijano, R. C.; Wang, S. K.; Hwang, H. C.** (1995): Fluid dynamics of venous valve closure. *Annals of Biomedical Engineering*, vol. 23, no. 6, pp. 750-759.
- Simão, M.; Ferreira, J. M.; Mora, R. J.; Ramos, H. M.** (2016): Identification of DVT diseases using numerical simulations. *Medical and Biological Engineering and Computing*, vol. 54, no. 10, pp. 1-19.
- Simmons, C. A.; Grant, G. R.; Manduchi, E.; Davies, P. F.** (2005): Spatial heterogeneity of endothelial phenotypes correlates with side-specific vulnerability to calcification in normal porcine aortic valves. *Circulation Research*, vol. 96, no. 7, pp. 792-799.
- Smiseth, O. A.; Thompson, C. R.; Lohavanichbutr, K.; Ling, H.; Abel, J. et al.** (1999): The pulmonary venous systolic flow pulse-its origin and relationship to left atrial pressure. *Journal of the American College of Cardiology*, vol. 34, no. 3, pp. 802-809.
- Smith, I. M.; Griffiths, D. V.; Margetts, L.** (2013): *Programming the Finite Element Method*. John Wiley & Sons.
- Soifer, E.; Weiss, D.; Marom, G.; Einav, S.** (2016): The effect of pathologic venous valve on neighboring valves: fluid-structure interactions modeling. *Medical and Biological Engineering and Computing*, vol. 55, no. 6, pp. 991-999.
- Sokolis, D. P.** (2008): Passive mechanical properties and constitutive modeling of blood vessels in relation to microstructure. *Medical and Biological Engineering and Computing*, vol. 46, no. 12, pp. 1187-1199.
- Tien, W. H.; Chen, H. Y.; Berwick, Z. C.; Krieger, J.; Chambers, S. et al.** (2014): Role of sinus in prosthetic venous valve. *European Journal of Vascular and Endovascular Surgery*, vol. 48, no. 1, pp. 98-104.
- Tien, W. H.; Chen, H. Y.; Berwick, Z. C.; Krieger, J.; Chambers, S. et al.** (2014): Characterization of a bioprosthetic bicuspid venous valve hemodynamics: implications for mechanism of valve dynamics. *European Journal of Vascular and Endovascular Surgery*, vol. 48, no. 4, pp. 459-464.

- Vukicevic, M.; Conover, T.; Jaeggli, M.; Zhou, J.; Pennati, G. et al.** (2014): Control of respiration-driven retrograde flow in the subdiaphragmatic venous return of the fontan circulation. *ASAIO Journal*, vol. 60, no. 4, pp. 391-399.
- Wang, X. S.; Yang, Y.; Wu, T.** (2019): Model studies of fluid-structure interaction problems. *Computer Modeling in Engineering & Sciences*, vol. 119, no. 1, pp. 5-34.
- Wang, X. S.; Wang, C.; Zhang, L. T.** (2012): Semi-implicit formulation of the immersed finite element method. *Computational Mechanics*, vol. 49, no. 4, pp. 421-430.
- Wang, X. S.; Zhang, L. T.** (2013): Modified immersed finite element method for fully-coupled fluid-structure interactions. *Computer Methods in Applied Mechanics and Engineering*, vol. 267, no. 1, pp. 150-169.
- Wesly, R. L.; Vaishnav, R. N.; Fuchs, J. C.; Patel, D. J.; Greenfield, J. C.** (1975): Static linear and nonlinear elastic properties of normal and arterialized venous tissue in dog and man. *Circulation Research*, vol. 37, no. 4, pp. 509-520.
- Whitmore, R. L.** (1968): *Rheology of the Circulation*. Oxford, New York.
- Yamaki, T.; Sasaki, K.; Nozaki, M.** (2002): Preoperative duplex-derived parameters and angioscopic evidence of valvular incompetence associated with superficial venous insufficiency. *Journal of Endovascular Therapy*, vol. 9, no. 2, pp. 229-233.
- Yao, J.; Liu, G. R.; Narmoneva, D. A.; Hinton, R. B.; Zhang, Z.** (2012): Immersed smoothed finite element method for fluid-structure interaction simulation of aortic valves. *Computational Mechanics*, vol. 50, no. 6, pp. 789-804.
- Zeng, X.; Li, S.** (2012): A three dimensional soft matter cell model for mechanotransduction. *Soft Matter*, vol. 8, no. 21, pp. 5765-5776.
- Zervides, C.; Giannoukas A. D.** (2013): Computational phlebology: reviewing computer models of the venous system. *Phlebology*, vol. 28, no. 4, pp. 209-218.
- Zhang, L.; Gerstenberger, A.; Wang, X.; Liu, W. K.** (2004): Immersed finite element method. *Computer Methods in Applied Mechanics and Engineering*, vol. 193, no. 21-22, pp. 2051-2067.
- Zhang, Z.; Liu, G. R.; Khoo, B. C.** (2013): A three dimensional immersed smoothed finite element method (3D IS-FEM) for fluid-structure interaction problems. *Computational Mechanics*, vol. 51, no. 2, pp. 129-150.

Appendix A

The N-S equations are discretized in the Petrov-Galerkin forms. With the velocity variation δv and the pressure variation δp , the weak form is written as

$$\int_{\Omega_f} \{ (\delta p + \tau^l \rho \delta v_{i,i}) v_{j,j} + [\delta v_i + \tau^c v_k \delta v_{i,k} + \tau^m \delta p_{,i}] [\rho (v_{i,t} + v_j v_{i,j}) - \rho g_i] \} d\Omega + \int_{\Omega_f} \delta v_{i,j} \sigma_{ij} d\Omega - \int_{\Gamma_{f,h}} \delta v_i h_i d\Gamma - \sum_{ie}^{ne} \int_{\Omega_{ne}^f} (\tau^c v_k \delta v_{i,k} + \tau^m \delta p_{,i}) \sigma_{ij,j} d\Omega = 0, \quad (A1)$$

where τ^c , τ^m and τ^l denote the three stabilized parameters in the Streamline-Upwind Petrov-Galerkin (SUPG) and Pressure-Stabilizing Petrov-Galerkin (PSPG) formulations.

In the standard Galerkin formulation, the unknowns v and p are discretized as

$$v_i = N_I v_{Ii}, \quad p = N_I p_I, \quad \delta v_i = N_I \delta v_{Ii}, \quad \delta p = N_I \delta p_I, \quad (A2)$$

where N_I is the shape function at arbitrary node I .

By substituting Eq. (A1) into Eq. (A2), we could obtain the discretized equilibrium equation at any node I ,

$$\begin{aligned} & \int_{\Omega^f} \{ (N_I \delta p_I + \tau^l \rho N_I \delta v_{Ii}) v_{j,j} + [N_I \delta v_{Ii} + \tau^c v_k N_{I,k} \delta v_{Ii} + \tau^m N_{I,i} \delta p_I] [\rho (v_{i,t} + \\ & v_j v_{i,j}) - \rho g_i] \} d\Omega + \int_{\Omega^f} N_{I,j} \delta v_{Ii} \sigma_{ij} d\Omega - \int_{\Gamma^{\epsilon,h}} N_I \delta v_{Ii} h_i d\Gamma - \\ & \sum_{ie}^{ne} \int_{\Omega_{ne}^f} (\tau^c v_k N_{I,k} \delta v_{Ii} + \tau^m N_{I,i} \delta p_I) \sigma_{ij,j} d\Omega = 0, \end{aligned} \quad (A3)$$

After extracting the common factors of δv_{Ii} and δp_I , Eq. (A1) could be rewritten as

$$\begin{aligned} & \delta v_{Ii} \left\{ \int_{\Omega^f} [\tau^l \rho N_I v_{j,j} + N_{I,j} \sigma_{ij} + \rho (N_I + \tau^c v_k N_{I,k}) (v_{i,t} + v_j v_{i,j} - g_i)] d\Omega - \right. \\ & \left. \int_{\Gamma^{\epsilon,h}} N_I h_i d\Gamma - \sum_{ie}^{ne} \int_{\Omega_{ne}^f} \tau^c v_k N_{I,k} \sigma_{ij,j} d\Omega \right\} + \delta p_I \left\{ \int_{\Omega^f} [N_I v_{j,j} + \tau^m N_{I,i} \rho (v_{i,t} + \right. \\ & \left. v_j v_{i,j}) - \rho g_i] d\Omega + \sum_{ie}^{ne} \int_{\Omega_{ne}^f} \tau^m N_{I,i} \sigma_{ij,j} d\Omega \right\} = 0, \end{aligned} \quad (A4)$$

Owing to the arbitrary variations of δv_{Ii} and δp_I , the equilibrium of the equivalent integral could deduce the following two equations:

$$\begin{aligned} & \int_{\Omega^f} [\tau^l \rho N_I v_{j,j} + N_{I,j} \sigma_{ij} + \rho (N_I + \tau^c v_k N_{I,k}) (v_{i,t} + v_j v_{i,j} - g_i)] d\Omega - \\ & \int_{\Gamma^{\epsilon,h}} N_I h_i d\Gamma - \sum_{ie}^{ne} \int_{\Omega_{ne}^f} \tau^c v_k N_{I,k} \sigma_{ij,j} d\Omega = 0, \end{aligned} \quad (A5)$$

$$\int_{\Omega^f} [N_I v_{j,j} + \tau^m N_{I,i} \rho (v_{i,t} + v_j v_{i,j}) - \rho g_i] d\Omega + \sum_{ie}^{ne} \int_{\Omega_{ne}^f} \tau^m N_{I,i} \sigma_{ij,j} d\Omega = 0, \quad (A6)$$

To solve the non-linear equations system, the Matrix-Free Krylov-Subspace method is employed with Newton iterations to approximate the true solution. And the generalized minimum residual (GMRES) method [Zhang, Gerstenberger, Wang et al. (2004)] was chosen as a Krylov subspace solver to solve the linear equations generated by the Newton iteration step. Then, the discretized residual equations of velocity r_{Ii}^v and pressure r_I^p at node I are written as below:

$$\begin{cases} r_{Ii}^v = \int_{\Omega} \{ \tau^l \rho N_{I,i} v_{j,j} + (N_{I,i} + \tau^c v_k N_{I,k}) [\rho (v_{i,t} + v_{i,j} v_{i,j}) - \sigma_{ij,j} - f_i] \} d\Omega \\ r_I^p = \int_{\Omega} \{ \tau^m N_{I,i} [\rho (v_{i,t} + v_{i,j} v_{i,j}) - \sigma_{ij,j} - f_i] + N_I v_{j,j} \} d\Omega \end{cases}, \quad (A7)$$

where r_{Ii}^v was the approximate residual on the left side of Eq. (A5) and r_I^p was that in Eq. (A6). And they could be also expressed as an implicit function $F(r_{Ii}^v, r_I^p) = 0$. In the numerical computation, the increments of the unknowns are iterated by the Newton-Raphson method till the true solution was finally approximated when it is convergent. Further derivation from can refer to Zhang et al. [Zhang, Gerstenberger, Wang et al. (2004)].

Appendix B

The finite element formulation of the solid dynamic equation is based on the Galerkin method. Following Eq. (11), the corresponding weak form is written as below:

$$\int_{\Omega^s} \delta d_i^s (\sigma_{ij,j}^s - \rho^s \ddot{d}_i^s - c \dot{d}_i^s - f_i^s) d\Omega = 0, \text{ on } \Omega^s \times [0, T] \quad (\text{B1})$$

where δd_i^s is the displacement variation or test function.

Assuming that the discretized formulations of the variable and variation are written as below:

$$d_i^s = N_I d_{Ii}^s, \delta d_i^s = N_I \delta d_{Ii}^s, \quad (\text{B2})$$

In the standard Galerkin method, Eq. (B2) can be substituted into Eq. (B3). Because the variation δd_{Ii}^s that is arbitrary, it could be eliminated. The semi-discrete form of the dynamic equation is then reformed as below:

$$\int_{\Omega^s} (N_I^T \rho^s N_J \ddot{d}_{Ii}^s + C_{IJ} \dot{d}_{Ii}^s + \nabla N_I^T D \nabla N_J d_{Ii}^s - N_I f_{ji}^s) d\Omega = 0 \quad (\text{B3})$$

where C_{IJ} is the damping matrix. It is used to consider the Rayleigh damping effect. The mass and stiffness matrices via the coefficients f_m and f_k , $C_{IJ} = f_m M_{IJ} + f_k K_{IJ}$.

Using the Newmark- β time integration formulation [Smith and Griffiths (2013)], then the acceleration and velocity should be expressed in the terms of the displacement. At arbitrary time t , Eq. (B3) is transformed into

$$\left[\left(f_m + \frac{1}{\theta \Delta t} \right) M_{IJ} + (f_k + \theta \Delta t) K_{IJ} \right] d_{Ii}^s = F_{ji}^s \quad (\text{B4})$$

with

$$\left\{ \begin{array}{l} M_{IJ} = \int_{\Omega^s} N_I^T \rho^s N_J d\Omega, \quad M'_{IJ} = \left(f_m + \frac{1}{\theta \Delta t} \right) \int_{\Omega^s} N_I^T \rho^s N_J d\Omega \\ K_{IJ} = \int_{\Omega^s} \nabla N_I^T D \nabla N_J d\Omega, \quad K'_{IJ} = (f_k + \theta \Delta t) \int_{\Omega^s} \nabla N_I^T D \nabla N_J d\Omega \\ F_{Ii}^s = \theta \Delta t F_{Ii}^t + \Delta F_1 + \Delta F_2 \\ \Delta F_1 = (1 - \theta) \Delta t F_{Ii}^{t-\Delta t} + \frac{1}{\theta} M_{IJ} \dot{d}_{Ii}^{s,t-\Delta t} \\ \Delta F_2 = + \left(f_m + \frac{1}{\theta \Delta t} \right) M_{IJ} d_{Ii}^{s,t-\Delta t} + [f_k - (1 - \theta) \Delta t] K_{IJ} d_{Ii}^{s,t-\Delta t} \end{array} \right. \quad (\text{B5})$$

where θ is a constant, Δt is the time step size, f_m and f_k are the damping coefficients, M_{IJ} is the mass matrix, and K_{IJ} is the stiffness matrix, M'_{IJ} and K'_{IJ} are the corresponding modified matrices.

In the solid solver, the mentioned matrices are formed by Cholesky factorization and are assembled in “skyline” form Smith et al. [Smith and Griffiths (2013)]. Subsequently, the Cholesky forward and back-substitution [Smith and Griffiths (2013)] are employed to solve the equation systems.

Appendix C

The venous wall and sinus are assumed as the linear elastic materials, and the corresponding stress is calculated as

$$\sigma_{ij}^{s,\text{wall}} = E \varepsilon_{ij}^{s,\text{wall}}, \text{ on } \Omega^{s,\text{wall}} \quad (\text{C1})$$

where $\varepsilon_{ij}^{s,wall}$ is the Cauchy strain and E is Young's modulus.

The venous valve is assumed as a hyperelastic material and calculated as

$$\sigma_{ij}^{s,valve} = J^{-1} F_{iI} S_{IJ} F_{jJ}^T, \text{ on } \Omega^{s,valve} \quad (C2)$$

where S_{IJ} is the second Piola-Kirchhoff stress and $F_{iI} (\partial x_i^s = \partial X_I^s)$ is the deformation gradient.

The hyperelastic material adopts a Mooney-Rivlin constitutive model, and the strain energy function $\mathcal{W}(I_c, II_c, III_c)$ is as follows

$$\mathcal{W} = c_1(I_c - 3) + c_2(II_c - 3) + c_3(III_c - 1)^2 \quad (C3)$$

where c_1, c_2 and c_3 are the three coefficients of the hyperelastic material, and I_c, II_c and III_c are three invariants of right hand Cauchy-Green strain tensor \mathbf{C} as shown below

$$I_c = \text{tr}\mathbf{C}, II_c = \text{tr}\mathbf{C}\mathbf{C}/2, III_c = \det\mathbf{C} = J^2 \quad (C4)$$

$$C_{IJ} = F_{iI} F_{iJ}^T, \quad (C5)$$

where $J = 1$ is satisfied for in the incompressible constitutive model and c_3 need not be considered.